

Calculation of the Energy Band Diagram of a Photoelectrochemical Water Splitting Cell

Peter Cendula,^{*,†} S. David Tilley,[‡] Sixto Gimenez,[§] Juan Bisquert,^{§,||} Matthias Schmid,[†] Michael Grätzel,[‡] and Jürgen O. Schumacher[†]

[†]Institute of Computational Physics, Zurich University of Applied Sciences (ZHAW), Wildbachstrasse 21, 8401 Winterthur, Switzerland

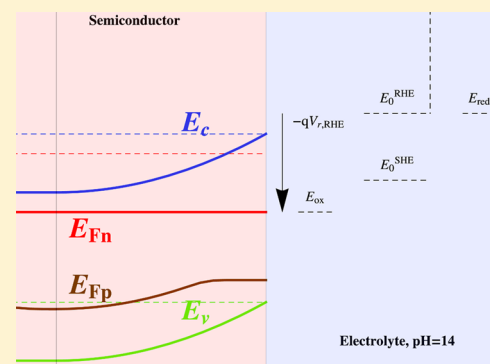
[‡]Laboratory of Photonics and Interfaces, Ecole Polytechnique Fédérale de Lausanne, EPFL-SB-ISIC-LPI, Station 6, 1015 Lausanne, Switzerland

[§]Photovoltaics and Optoelectronic Devices Group, Department of Physics, University Jaume I, 12071 Castellon, Spain

^{||}Department of Chemistry, Faculty of Science, King Abdulaziz University, Jeddah 21589, Saudi Arabia

S Supporting Information

ABSTRACT: A physical model is presented for the semiconductor electrode of a photoelectrochemical cell. The model accounts for the potential drop in the Helmholtz layer and thus enables description of both band edge pinning and unpinning. The model is based on the continuity equations for charge carriers and direct charge transfer from the energy bands to the electrolyte. A quantitative calculation of the position of the energy bands and the variation of the quasi-Fermi levels in the semiconductor with respect to the water reduction and oxidation potentials are presented. Calculated photocurrent–voltage curves are compared with established analytical models and experimental data. Our model calculations are suitable to enhance understanding and improve the properties of semiconductors for photoelectrochemical water splitting.



INTRODUCTION

Research on hydrogen production with photoelectrochemical (PEC) cells is propelled by the worldwide quest for capturing, storing, and using solar energy instead of the decreasing fossil energy reserves. Hydrogen is widely considered as a key solar fuel of the future.¹ Hydrogen is also part of power-to-gas conversion systems developed to resolve the intermittency in wind and solar energy production.² Although a PEC/photo-voltaic cell with 12.4% efficiency was demonstrated with GaInP₂/GaAs,³ decreasing its cost and increasing its lifetime remain a challenge. An alternative approach often pursued is to use abundant and cheap metal oxides as the semiconductor materials for PEC electrodes.^{4–6} However, their recombination losses, charge carrier conduction, and water oxidation properties need to be understood and optimized both by measurement and numerical simulation in order to further advance these materials.⁷

Several approaches for a mathematical analysis of semiconductor electrodes can be found in the literature, including analytical^{8,9} and numerical models^{10,11} of PEC cells. An extensive numerical study of PEC behavior of Si and GaP nanowires was recently conducted with commercial software.¹² Since surface states play a major role for many semiconductors, corresponding models were also developed to analyze their effect on the electrochemical measurements.^{13–15} On the PEC system level, models of the coupled charge and species

conservation, fluid flow, and electrochemical reactions were recently developed.^{16,17} The latter studies revealed how PEC systems should be designed with minimal resistive losses and low crossover of hydrogen and oxygen by use of a nonpermeable separator.

Almost every publication on PEC cells features a schematic energy band diagram of a PEC cell, mostly sketched by hand from basic physical understanding described in textbooks on electrochemistry.^{7,18,19} Although such sketches might be qualitatively correct, numerical calculations of the charge carrier transport might reveal additional features not captured by the sketches. We are aware that the development of numerical calculations is frequently hindered by the complicated physical processes in the actual materials and lack of measurements of parameter values for these processes.²⁰ In spite of these obstacles, we think that the recent advent of user-friendly numerical software and advanced measurement techniques could fill the gap between the experimental and numerical approaches.

Received: September 25, 2014

Revised: November 15, 2014

Published: November 16, 2014

MODEL

In this work, we present calculations of the energy band diagram of a PEC electrode from a physical model with clearly formulated assumptions.²¹ The model is based on charge carrier continuity equations with direct charge transfer from the valence or conduction band to the electrolyte. We consider a PEC cell consisting of a thin compact n-type semiconductor; hence, PEC cells with porous structures^{22,23} are not directly described with our model. We assume an electrolyte that can easily accept a single electron or hole (such as H_2O_2 ²⁴ or $[\text{Fe}(\text{CN})_6]^{3-/4-25}$). Charge transfer occurs across the semiconductor/electrolyte interface until an equilibrium charge distribution is reached and the equilibrium Fermi level in the semiconductor E_{F0} becomes equal to the redox Fermi level E_{redox}

$$E_{F0} = E_{\text{redox}} \quad (1)$$

We reserve subscript 0 for equilibrium values in the dark in the following. To derive our model, we use and repeat some of the general definitions introduced in our previous work²⁶ to describe the PEC cell in steady state under illumination (out of equilibrium), Figure 1 and Table 1. Note that we use a notation

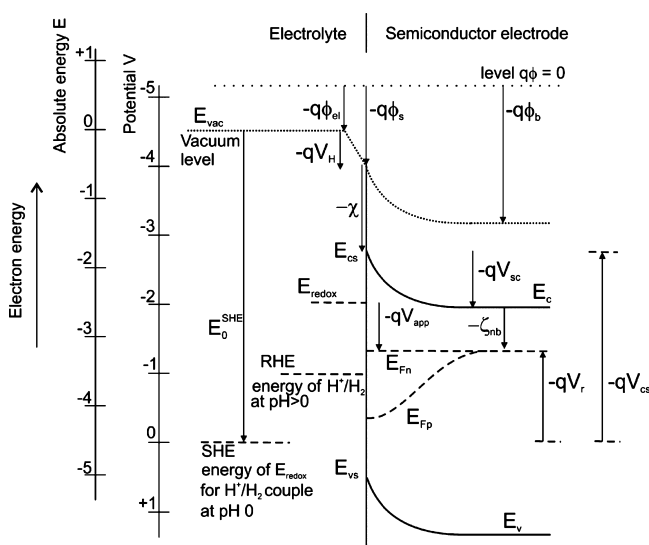


Figure 1. Scheme of an n-type semiconductor electrode in steady state under illumination, with electron energy indicated in the absolute energy scale (with respect to the vacuum level), and potentials in the electrochemical scale, with respect to SHE. Reprinted with permission from ref 26. Copyright 2014 American Chemical Society.

of subscript sc for semiconductor, s for surface quantity, and b for a bulk semiconductor quantity (where electrons and hole remain at equilibrium in the dark).

Bulk equilibrium properties of the isolated semiconductor are denoted with a subscript 0i. The bulk of the semiconductor is electrically neutral; hence, the concentration of electrons in the bulk n_{0i} must be equal to the number of fully ionized donors N_D , $n_{0i} = N_D$ (for $N_D \gg n_i$). Thus, the concentration of holes is $p_{0i} = n_i^2/n_{0i}$, where n_i denotes intrinsic carrier concentration. An isolated unbiased semiconductor before contact to an electrolyte has a conduction band edge $E_{c,0i}$ and a Fermi level $E_{F,0i}$ related to the vacuum level E_{vac} and to the electron affinity χ by

$$E_{c,0i} = E_{\text{vac}} - \chi \quad (2)$$

$$E_{F,0i} = E_{c,0i} - \zeta_{\text{nb}} \quad (3)$$

$$\zeta_{\text{nb}} = k_B T \ln \left(\frac{N_C}{n_{0i}} \right) \quad (4)$$

where k_B is the Boltzmann constant, T is the temperature, q is the elementary charge, N_C is the effective density of states in the conduction band, and ζ_{nb} is the distance of the conduction band edge to the Fermi level. In the following, we use $E_{\text{vac}} = 0$ eV as the usual convention. The potential drop in the Helmholtz layer in the dark V_H is calculated from the local vacuum level (LVL) at the surface of the semiconductor ($-q\phi_s$) and the LVL of the electrolyte ($-q\phi_{\text{el}}$), Figure 1,

$$-qV_H = -q\phi_s - (-q\phi_{\text{el}}) \quad (5)$$

Note that the potential drop in the Helmholtz layer can be a different value at the flatband situation (denoted V_H^{fb}) than that at the other measured voltage (denoted V_H). We measure the voltage V_r of the semiconductor electrode with respect to a reference electrode, which is the difference of the Fermi level of electrons in the semiconductor back-contact $E_{F_{\text{bc}}}$ and the Fermi level of the reference electrode E_0^{SHE}

$$V_r = -\frac{E_{F_{\text{bc}}} - E_0^{\text{SHE}}}{q} \quad (6)$$

In this work, we use both the standard hydrogen electrode (SHE) energy and the reversible hydrogen electrode (RHE) as reference electrodes and the scale of the energy. The measured voltage with respect to the SHE is denoted V_r (without subscript SHE) and the measured voltage with respect to the RHE $V_{r,\text{RHE}}$ with

$$V_{r,\text{RHE}} = V_r + 2.3V_{\text{th}}\text{pH} \quad (7)$$

where $V_{\text{th}} = (k_B T/q)$ is the thermal voltage and pH denotes the pH value of the solution. We draw attention to the fact that negative bias versus RHE brings the energy closer to the vacuum level E_{vac} . The position of the electron Fermi level at the semiconductor back-contact is calculated as (see Figure 1)

$$E_{F_{\text{bc}}} = -qV_H - \chi - qV_{\text{sc}} - \zeta_{\text{nb}} \quad (8)$$

where V_{sc} denotes the potential drop in the semiconductor. What is usually reported in the literature is the value of the flatband potential, which is the measured voltage when the bands are flat ($V_{\text{sc}} = 0$)

$$V_{\text{fb}} = V_r|_{V_{\text{sc}}=0} = \frac{E_0^{\text{SHE}} + \chi + \zeta_{\text{nb}}}{q} + V_H^{\text{fb}} \quad (9)$$

The value of V_H^{fb} is often not known as it depends on the surface conditions of the semiconductor in the electrolyte. For this work, we use the known values of V_{fb} and χ and we determine V_H^{fb} from eq 9. The potential drop in the semiconductor V_{sc} can be expressed from Figure 1 as

$$-qV_{\text{sc}} = -q\phi_b - (-q\phi_s) \quad (10)$$

Then from eqs 6, 8, and 9 follows

$$V_{\text{sc}} = V_r - V_{\text{fb}} - (V_H - V_H^{\text{fb}}) \quad (11)$$

The second option is to refer the voltage to the equilibrium of the semiconductor/electrolyte interface (SEI), and this value is denoted $V_{\text{app}}^{\text{SEI}}$

Table 1. Table of Symbols and Abbreviations^a

symbol	unit	description	symbol	unit	description
CE		counter electrode	E_{ox}	eV	standard water oxidation energy
LVL		local vacuum level	E_{F0}	eV	equilibrium Fermi level in the semiconductor (dark)
PEC		photoelectrochemical	$E_{c,0i}$	eV	conduction band edge in the isolated semiconductor before contact to an electrolyte
SCR		space charge region	$E_{F,0i}$	eV	Fermi level in the isolated semiconductor before contact to an electrolyte
SEI		semiconductor/electrolyte interface	E_{Fn}, E_{Fp}	eV	quasi-Fermi energy of electrons and holes
SHE		standard hydrogen electrode	$E_{Fn,bc}$	eV	quasi-Fermi energy of electrons at the back-contact
SI		Supporting Information	E_c	eV	conduction band edge in the semiconductor
RHE		reversible hydrogen electrode	E_{cs}	eV	conduction band edge at the SEI
subscript i		quantity in the isolated semiconductor before contact to an electrolyte	E_v	eV	valence band edge in the semiconductor
subscript b		quantity in the semiconductor bulk	E_{vs}	eV	valence band edge at the SEI
subscript s		quantity at the SEI	$E_{F,CE}$	eV	Fermi level of the CE
k_B	eV/K	Boltzmann constant (8.6×10^{-5} eV/K)	ζ_{nb}	eV	difference between the semiconductor conduction band energy and the electron Fermi level
T	K	temperature (300 K)	ϕ	V	local electrostatic potential
q	C	elementary charge (1.6×10^{-19} C)	ϕ_a	V	approximate solution for local electrostatic potential
V_{th}	V	thermal voltage (25.9 mV)	ϕ_{el}	V	local electrostatic potential of the electrolyte
h	J·s	Planck's constant (6.62607×10^{-34} J·s)	ϕ_s	V	Local electrostatic potential at SEI
c	m/s	speed of light in vacuum (299792458 m/s)	ϕ_b	V	Local electrostatic potential in the semiconductor bulk
V_r	V	measurable voltage with respect to SHE reference electrode	n_i	m ⁻³	intrinsic carrier concentration in the bulk of the semiconductor
$V_{r,RHE}$	V	measurable voltage with respect to RHE	n_{0i}, p_{0i}	m ⁻³	equilibrium concentration of electrons and holes in the bulk of isolated semiconductor
$V_{r,RHE}^{inv}$	V	measurable voltage with respect to RHE when the inversion layer starts to form	n_{dark}, p_{dark}	m ⁻³	dark concentration of electrons and holes
V_{fb}	V	flatband voltage with respect to SHE	n, p	m ⁻³	concentration of electrons and holes
$V_{fb,RHE}$	V	flatband voltage with respect to RHE	w	m	width of the space-charge region in the semiconductor
V_{app}	V	applied voltage to the semiconductor with respect to the dark equilibrium (unbiased)	j_h	A/m ²	hole current density
V_H	V	potential (voltage) drop across the Helmholtz layer in the dark	j_G	A/m ²	photocurrent density calculated by Gärtner ⁸
V_H^{fb}	V	potential (voltage) drop across the Helmholtz layer at flatband situation in the dark	j_R	A/m ²	photocurrent density calculated by Reichmann ¹⁰
V_{H0}	V	potential (voltage) drop across the Helmholtz layer in the dark equilibrium	j_{sat}	A/m ²	saturation current density
V_{sc}	V	potential (voltage) drop across the semiconductor	G_{tr}, R_h	m ⁻³ s ⁻¹	generation and recombination rate of holes
V_{cs}	V	potential of the conduction band at the SEI	P	m ⁻² s ⁻¹	no. of photons absorbed in the semiconductor from AM1.5G spectrum
V_{bi}	V	built-in voltage of semiconductor/liquid junction	Φ	m ⁻³ s ⁻¹	spectral photon flux of AM1.5G spectrum
V_{CE}	V	voltage between the reference electrode and counter electrode	μ_h	m ² V ⁻¹ s ⁻¹	mobility of holes
η	V	electrochemical overpotential at the CE	D_h	m ² s ⁻¹	diffusion constant of holes
E_{vac}	eV	energy of the local vacuum level	k_{trh}	ms ⁻¹	rate constant for charge transfer of VB holes to electrolyte
E_0^{SHE}	eV	energy of the SHE with respect to vacuum level of the electron (−4.44 eV)	λ_g	m	wavelength below which semiconductor absorbs photons
E_0^{RHE}	eV	energy of the RHE with respect to vacuum level of the electron	r_s	ms ⁻¹	back-contact surface recombination velocity
E_{redox}	eV	Fermi level of the electrolyte species (redox level)			
E_{red}	eV	standard water reduction energy			

^aSymbols for material parameters are defined in Table 2.

$$V_{app} = -\frac{E_{Fn,bc} - E_{redox}}{q} \quad (12)$$

$$V_{app} = V_{sc} - V_{bi} + V_H - V_{H0} \quad (13)$$

where the built-in voltage is denoted V_{bi} and the potential drop across the Helmholtz layer in the dark equilibrium V_{H0} . The equilibrium of SEI means $V_{app} = 0$ V.

On the semiconductor side of the junction, the electrostatic potential ϕ is obtained by solving Poisson's equation¹⁹

$$\frac{d^2\phi}{dx^2} = -\frac{q(N_D - n(x) + p(x))}{\epsilon_0\epsilon_r} \quad (14)$$

where ϵ_0 is the permittivity of vacuum, ϵ_r is the relative permittivity of the semiconductor, N_D is the concentration of

fully ionized donors, $n(x)$ is the concentration of free electrons, and $p(x)$ is the concentration of free holes ($p(x) \ll n(x)$ (for n-type semiconductor in the dark)). We can write for the conduction and the valence band edge energies E_c and E_v in the electrostatic potential $\phi(x)$

$$E_c(x) = -\chi - q(\phi(x) - \phi_{el}) \quad (15)$$

$$E_v(x) = E_c(x) - E_g$$

where the bandgap energy of the semiconductor is E_g . Band edge pinning (constant value of E_{cs} and E_{vs} for any measured voltage) is present if $V_H = V_H^{fb}$ for any measured voltage; otherwise the band edges become unpinning (values of E_{cs} and E_{vs} vary with measured voltage).

A simple approximation to solve Poisson's equation, eq 14, is to assume that the total space charge is uniformly distributed

inside the space charge region (SCR) of width w (also called the depletion region approximation)

$$w = \sqrt{\frac{2\epsilon_0\epsilon_r}{eN_D}|V_{sc}|} \quad (16)$$

The boundary conditions for the electrostatic potential ϕ follow directly from the definitions in Figure 1

$$\phi(0) = \phi_s \quad (17)$$

$$\phi(w) = \phi_b \quad (18)$$

The concentration of free electrons and holes in the dark $n_{\text{dark}}(x)$ and $p_{\text{dark}}(x)$ can be written as

$$n_{\text{dark}}(x) = n_{0i} \exp\left[\frac{\phi(x) - \phi_b}{V_{th}}\right] \quad (19)$$

$$p_{\text{dark}}(x) = p_{0i} \exp\left[\frac{-\phi(x) + \phi_b}{V_{th}}\right] \quad (20)$$

The value of the electrostatic potential in the semiconductor bulk ϕ_b appears in the preceding expressions because we have made a general definition of the electrostatic potential including the potential drop in the Helmholtz layer. Therefore, ϕ_b is not zero, in contrast to a recent textbook definition.⁷ The approximate solution of Poisson's eq ϕ_a is then

$$\phi_a(x) = \phi_b - \text{sign}(V_{sc}) \frac{qN_D}{2\epsilon_0\epsilon_r}(w-x)^2, \quad 0 < x < w \quad (21)$$

$$\phi_a(x) = \phi_b, \quad w < x < d$$

When the measured voltage V_r is positive of the flatband potential V_{fb} , the n-type semiconductor is in the depletion regime. When the measured voltage is negative of the flatband potential, the semiconductor is in the accumulation regime (due to the sign of V_{sc}).

In the following analysis, we neglect reflection losses and absorption in the electrolyte. Both illumination directions from electrolyte–electrode (EE) or substrate–electrode (SE) are included with the generation rate of charge carriers given by the simple Lambert–Beer law $G_h(x) = \alpha P e^{-\alpha x}$ for EE illumination or $G_h(x) = \alpha P e^{-\alpha(d-x)}$ for SE illumination. The number of photons with energy above $E_g = (hc/\lambda_g)$ that are absorbed in the semiconductor is $P = \int_{\lambda_{\min}}^{\lambda_g} \Phi(\lambda) d\lambda$, the spectral photon flux of standard AM1.5G spectrum with intensity of 100 mW/cm²²⁷ is $\Phi(\lambda)$ and the absorption coefficient of the semiconductor is α . We assume low-injection conditions with the number of photogenerated electrons smaller than the donor concentration. Hence, the electron concentration is roughly equal to the dark electron concentration $n(x) = n_{\text{dark}}(x)$. The hole continuity equation is solved to obtain the free hole concentration p inside of the semiconductor of thickness d

$$0 = -\frac{1}{q} \frac{\partial j_h}{\partial x} + G_h(x) - R_h(x) \quad (22)$$

The hole current density j_h is expressed using the analytical solution of Poisson's equation

$$j_h = -qD_h \frac{\partial p}{\partial x} - q\mu_h p \frac{\partial \phi_a}{\partial x} \quad (23)$$

where $\mu_h = (qD_h)/(k_B T)$ is the hole mobility, and D_h is the hole diffusion constant. Direct band-to-band nonlinear recombination is assumed.

$$R_h = \frac{1}{N_D \tau_h} (n_{\text{dark}} p - n_i^2) \quad (24)$$

We assume that charge transfer under illumination occurs exclusively from the valence band to the electrolyte. We do not include charge transfer from surface states in the current analysis. The current density of valence band holes at the SEI is described by a first-order approximation²⁸

$$j_h(0) = -qk_{trh}(p(0) - p_{\text{dark}}(0)) \quad (25)$$

where k_{trh} is the rate constant for hole transfer, and a linear dependence on the difference of the interfacial hole concentration $p(0)$ from its dark value $p_{\text{dark}}(0)$ at the interface is assumed. Since the thickness of the semiconductor is in the order of the penetration length of light α^{-1} for the hematite parameters listed in Table 2, we consider the hole current at the

Table 2. Material Parameters of Semiconductors Used in the Calculations

symbol	Fe ₂ O ₃ ³⁹	Cu ₂ O ^{42,45}	description
N_D (cm ⁻³)	2.91×10^{18}	0	donor concentration
N_A (cm ⁻³)	0	5×10^{17}	acceptor concentration
$V_{fb,RHE}$ (V)	+0.5	+0.8	flatband potential
χ (eV)	+4.78 ^{46,47}	+4.22 ⁴⁶	electron affinity
N_C (cm ⁻³)	$4 \times 10^{22,48,49}$	1.1×10^{19}	density of states of CB
N_V (cm ⁻³)	1×10^{22}	1.1×10^{19}	density of states of VB
ϵ_r	32 ⁵⁰	6.6	relative permittivity
E_g (eV)	2.1	2.17	bandgap energy
d (nm)	33	325	thickness of semiconductor
τ_e (ns)		0.25	electron lifetime
τ_h (ns)	0.048 ⁵¹		hole lifetime
L_e (nm)		40	electron diffusion length
L_h (nm)	5 ⁷		hole diffusion length
α (cm ⁻¹)	1.5×10^5	1.3×10^4	absorption coefficient
pH	14	4.9	pH value of the electrolyte

back contact of the semiconductor to depend on a surface recombination velocity r_s .

$$j_h(d) = +qr_s(p(d) - p_{0i}) \quad (26)$$

We use $r_s = 10^5$ m/s for numerical calculations throughout this work.¹² In order to obtain convergence of the numerical solution procedure, the continuity equation was solved in a nondimensional form after applying the usual normalization of the variables of the drift-diffusion equations.²⁹

The quasi-Fermi energies E_{Fn} and E_{Fp} under the influence of an electrostatic potential $\phi(x)$ are calculated by the Boltzmann distribution

$$n(x) = N_C \exp\left(-\frac{E_C(x) - E_{Fn}}{k_B T}\right) \quad (27)$$

$$p(x) = N_V \exp\left(-\frac{E_{Fp} - E_V(x)}{k_B T}\right) \quad (28)$$

RESULTS AND DISCUSSION

We numerically solved the hole (electron) continuity eq 22 for an n-type (p-type) semiconductor by using the depletion region approximation of the electrostatic potential eq 21. The results upon EE illumination for the n-type Fe_2O_3 and the p-type Cu_2O are presented in the following. If not otherwise stated, we assume $\phi_{\text{el}} = 0$ V and band edge pinning ($V_{\text{H}}^{\text{fb}} = V_{\text{H}0} = V_{\text{H}}$) in the following.

Our work for simplicity does not include the effect of electrocatalyst on the photoelectrode surface, even though its use is undoubtedly necessary for practical devices.³⁰ Recently, a numerical model to describe realistic electrocatalysts with various porosity and ion permeability appeared.³¹ The main conclusion of ref 31 is that the adaptive and metallic catalysts differ mainly with respect to the (electrostatic) potential drop. For the adaptive catalyst the potential drop develops only in the semiconductor, whereas for the metallic catalyst the potential drop develops both in the electrolyte and in the semiconductor. Our model already assumes that the potential drop is prescribed as a material/interface parameter; hence, both adaptive and metallic catalysts of ref 31 can be included in our model by defining the value of this potential drop.

Fe_2O_3 . The charge carrier concentration profiles calculated from the model are plotted in Figure 2. In the dark, the SCR is depleted of electrons and the concentration of holes is larger than the bulk hole concentration. For increasing $V_{\text{r,RHE}}$, the

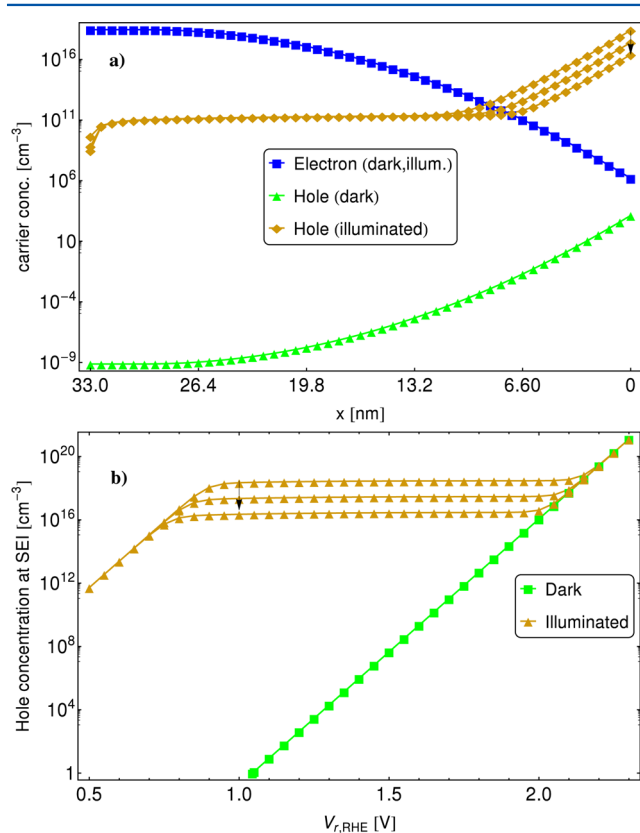


Figure 2. (a) Simulated charge carrier concentrations in the semiconductor for the measured voltage of $V_{\text{r,RHE}} = 1.23$ V. Note the reverse orientation of the horizontal axis (also in Figure 3 and Figure 5) compared to Figure 1. (b) Hole concentration at the SEI as a function of $V_{\text{r,RHE}}$. The directions of the arrows mean increasing $k_{\text{th}} = 10^{-4}$, 10^{-3} , and 10^{-2} m/s. The parameters for hematite from Table 2 were used.

dark electron concentration at the SEI $n_{\text{dark}}(0)$ decreases until it is smaller than the dark hole concentration at the SEI $p_{\text{dark}}(0)$, leading to an inversion layer characterized by larger concentration of holes (minorities) than electrons (majorities) in the SCR. The corresponding value of $V_{\text{sc}}^{\text{inv}} = V_{\text{th}} \ln(N_{\text{D}}/n_1) = 0.88$ V and thus $V_{\text{r,RHE}}^{\text{inv}} = 1.4$ V are obtained. Therefore, a more detailed future model should take into account the electron continuity equation instead of assuming that the electron concentration upon illumination is equal to the electron concentration in the dark.

Upon illumination, the concentration of electrons is equal to the dark electron concentration. Fewer holes are accumulated near the SEI for increasing rate constant k_{th} (faster charge transfer), Figure 2. For large $V_{\text{r,RHE}}$ (>2.0 V), the hole concentration upon illumination near the SEI approaches the hole concentration in the dark, Figure 2b. At the back-contact, the hole concentration follows from the solution of the continuity equation and the boundary condition in eq 26.

The energy band diagram is shown for a three-electrode measurement setup in Figure 3. The measured voltage of $V_{\text{r,RHE}} = 1.23$ V is assumed, which is a standard voltage used for the comparison of the different PEC electrodes.^{32,35} The measured voltage $V_{\text{r,RHE}}$ is indicated in Figure 3a) with an arrow on the energy scale, $-qV_{\text{r,RHE}}$. This notation is explained in our previous work.²⁶ The band edges of the semiconductor $E_{\text{c}}(x), E_{\text{v}}(x)$ for the flatband condition ($V_{\text{r,RHE}} = V_{\text{fb,RHE}}$) are shown as dashed lines, whereas those away from the flatband condition ($V_{\text{r,RHE}} \neq V_{\text{fb,RHE}}$) are shown as solid lines. The band positions at the flatband conditions for hematite agree well with the values reported for pH = 1^{34,35} and pH = 14.²³ An upward band bending of the semiconductor is present if $V_{\text{r,RHE}}$ is more positive than $V_{\text{fb,RHE}}$; see Figure 3. The band edges are pinned at the SEI by default (since we assume $V_{\text{H}} = V_{\text{H}}^{\text{fb}}$), but we allow for the modification of the surface conditions by changing the value of V_{H} in our interactive band diagram software.²¹

The number of photogenerated electrons is small compared to the donor concentration, and thus the illumination does not change the electron concentration. Therefore, the electron quasi-Fermi level E_{Fn} is constant across the semiconductor, eq 27, and $E_{\text{Fn}} = E_{\text{Fn,bc}}$. The position of E_{Fn} relative to E_0^{RHE} in the energy diagram is given by the arrow $-qV_{\text{r,RHE}}$, eq 8. In contrast, the hole concentration is determined mainly by photogenerated holes that are re-distributed in the semiconductor according to the continuity eq 22. Since $E_{\text{v}}(0)$ is more positive than E_{ox} , the transfer of holes from the valence band can thermodynamically oxidize the electrolyte species. The external wire electrically connects the semiconductor to the metal counter electrode (CE) through the potentiostat. The counter electrode Fermi level $E_{\text{F,CE}}$ is automatically adjusted by applying the voltage V_{CE} above the water reduction energy E_{red} (including the electrochemical overpotential η) by the potentiostat to enable hydrogen evolution at the counter electrode. The counter electrode is shown in the energy diagram only to completely describe the three-electrode setup, and we ignore its polarization in the following.³⁶ In the electrolyte, we plot the two reference electrode energies E_0^{SHE} and E_0^{RHE} , the standard water reduction and oxidation energy E_{red} (0 eV vs RHE) and E_{ox} (1.23 eV vs RHE). Note that the relation of E_{red} and E_{ox} to E_{redox} depends on the concentrations (activities) of oxidizing and reducing species in the solution.³⁷

The energy band diagram in the semiconductor for different values of the measured voltage $V_{\text{r,RHE}}$ is plotted in Figure 3b. For increasing $V_{\text{r,RHE}}$ the band bending increases and the

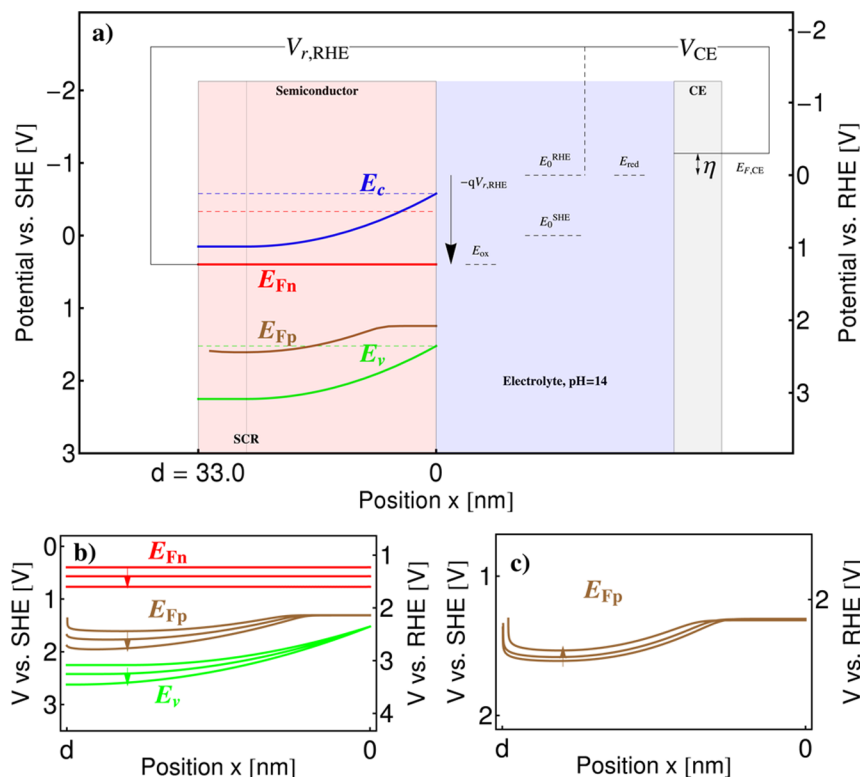


Figure 3. (a) Calculated energy band diagram of the n-doped hematite at $V_{r,RHE} = 1.23$ V and upon AM1.5G sunlight illumination. The semiconductor thickness is denoted d , the semiconductor/electrolyte interface is at $x = 0$ nm, and the counter electrode is indicated by CE on the right-hand side. The value of $k_{th} = 10^{-3}$ m/s is assumed for the rate constant of charge transfer of valence band holes to the electrolyte. Other material parameters are listed in Table 2. The interactive software tool to calculate the energy band diagram can be downloaded at <http://icp.zhaw.ch/PEC>. (b) Quasi-Fermi level diagram, where the arrows indicate the increasing values of the measured voltage, $V_{r,RHE} = 1.23, 1.4$, and 1.6 V. (c) Influence of the minority carrier diffusion length L_h on the quasi-Fermi level E_{Fp} of holes, where the arrow indicates increasing values of $L_h = 5, 10$, and 25 nm.

electron quasi-Fermi level E_{Fn} shifts down on the RHE scale. Interestingly, the hole quasi-Fermi level $E_{Fp}(0)$ at the SEI remains nearly constant for increasing $V_{r,RHE}$ (see Figure S1 in the Supporting Information) and thus the splitting of the quasi-Fermi levels approaches zero. In the neutral region $w < x < d$, the hole quasi-Fermi level $E_{Fp}(x)$ is more negative for increasing $V_{r,RHE}$, and the photovoltage is nearly constant. When the hole diffusion length $L_h = (D_h\tau_h)^{1/2}$ is increased, the flat region of the hole quasi-Fermi level E_{Fp} near the SEI is enlarged, Figure 3c, and the hole concentration in the neutral region decreases (see Figure S2 in the Supporting Information).

We simulated the photocurrent–voltage curves with our numerical model $j_h(0)$ (eq 25) and compared the results with the published models of Gärtner⁸ and Reichmann,¹⁰ Figure 4. According to the Gärtner model, the minority charge carrier concentration is calculated from the diffusion equation, neglecting recombination in the SCR and assuming that every hole in SCR contributes to the photocurrent (infinitely fast hole/electron transfer to the electrolyte). The photocurrent density of Gärtner is

$$j_G = eP \left(1 - \frac{e^{-\alpha w}}{1 + \alpha L_h} \right) \quad (29)$$

Therefore, j_G overestimates the minority carrier photocurrent in comparison to our numerical model $j_h(0)$. The recombination in the SCR by the Sah–Noyce–Shockley formalism was incorporated into the model by Reichmann¹⁰ with resulting

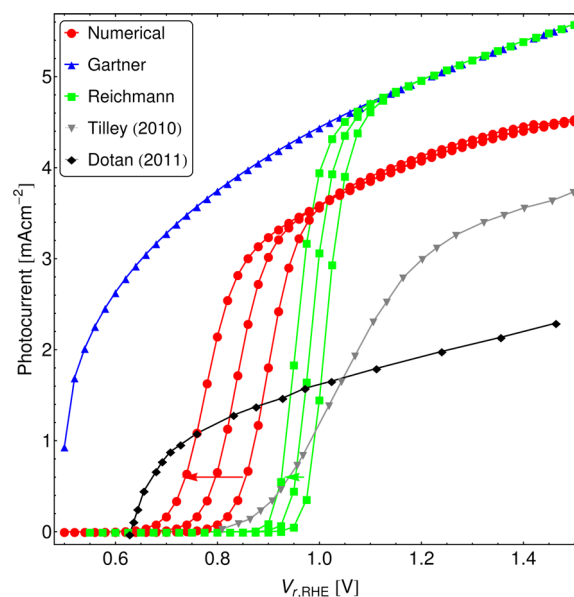


Figure 4. Photocurrent–voltage curves for $k_{th} = 10^{-4}, 10^{-3}$, and 10^{-2} m/s (in direction of arrows) from our numerical model, the Gärtner model, the Reichmann model, and the measured data from Tilley et al.³⁸ and Dotan et al.²⁴ for the n-doped hematite and other material parameters listed in Table 2.

photocurrent j_R (the detailed expression is given in the Supporting Information). For small $V_{r,RHE}$, j_R is much smaller

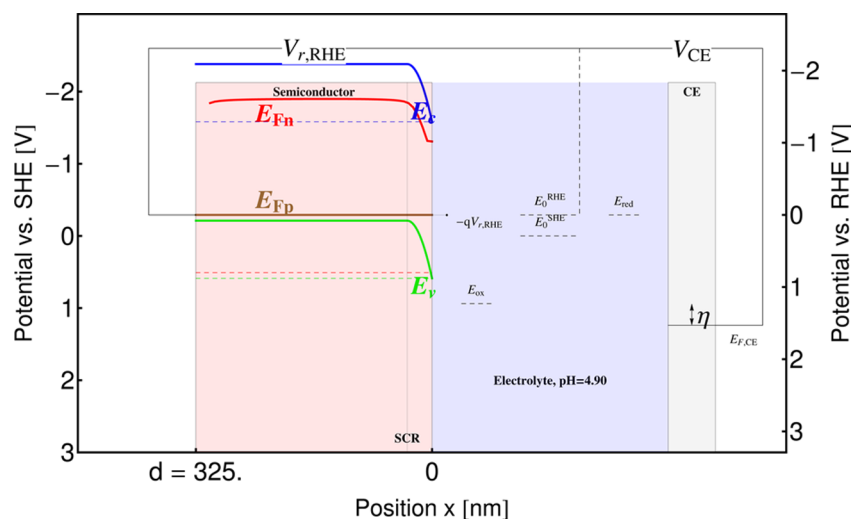


Figure 5. Calculated energy band diagram for the p-doped Cu_2O , $k_{\text{tre}} = 10 \text{ m/s}$ and $V_{\text{r,RHE}} = 0 \text{ V}$ (hence the voltage arrow is not visible in the diagram). The material parameters are listed in Table 2. The interactive tool for calculation of this figure can be accessed at <http://icp.zhaw.ch/PEC>.

than j_{G} because the SCR recombination loss is included in j_{R} . The onset of the photocurrent calculated by Reichmann j_{R} starts when $\gamma = j_{\text{satn}} e^{-V_{\text{app}}/V_{\text{th}}/qk_{\text{trh}}p_{\text{dark}}(0)} \approx 1$ (j_{satn} is the saturation current density as defined in the Supporting Information). Therefore, if we consider faster charge transfer kinetics (larger k_{trh}), we need a smaller value of the onset potential $V_{\text{r,RHE}}$ (and thus V_{app}) to obtain a similar value $\gamma \approx 1$. For increasing $V_{\text{r,RHE}}$, j_{R} approaches j_{G} because the SCR recombination becomes negligible in j_{R} ,¹⁰ but the numerical photocurrent $j_{\text{h}}(0)$ is smaller than j_{G} since the SCR recombination is included in $j_{\text{h}}(0)$. The numerical photocurrent $j_{\text{h}}(0)$ onsets when $V_{\text{r,RHE}}$ is more positive than $V_{\text{fb,RHE}}$ and it is larger than j_{R} for small $V_{\text{r,RHE}}$. Increasing the rate constant k_{trh} represents a faster exchange rate of holes with the solution. This also shifts the numerical j - V curve to the left as predicted by the Reichmann model, decreasing the onset potential of the photocurrent.

The measured photocurrent–voltage (IV) responses of the nanostructured APCVD hematite in H_2O_2 ²⁴ and NaOH ³⁸ electrolyte are compared with the prediction from our model in Figure 4. The IV profile from ref 24 appears similar to the Gärtner model but shifted to lower photocurrents. In addition, the onset potential in ref 24 is about 0.1 V more negative than in the numerical model. Measurements in ref 38 were done on the electrode with IrO_2 catalyst. The onset voltage $\approx 0.8 V_{\text{RHE}}$ of the measured photocurrent³⁸ is approximately reproduced with the simulated photocurrent for the rate constant of $k_{\text{trh}} = 10^{-4} \text{ m/s}$. However, the slope of the measured photocurrent and its value 4.3 mA/cm^2 at $1.5 V_{\text{r,RHE}}$ are smaller than the slope of the simulated photocurrent and its value 3.8 mA/cm^2 at $1.5 V_{\text{r,RHE}}$.

These differences in the simulated and the measured photocurrent^{24,38} can be understood by discussing the assumptions of our model with respect to refs 24 and 38, where the donor concentration was roughly $N_{\text{D}} \approx 10^{20} \text{ cm}^{-3}$, which is nearly 2 orders of magnitude larger than the donor concentration $N_{\text{D}} = 2.91 \times 10^{18} \text{ cm}^{-3}$ assumed in this work, Table 2. The main reason we chose parameters from ref 39 was the uniformity of the hematite film obtained (without nanostructures) and its constant thickness that corresponds well to our model. In addition, hematite in refs 24 and 38 is highly nanostructured (as compared to our compact film assumption) with varying thickness of the hematite cauliflower

structures and increased light absorption due to the trapping of light in the nanostructure. Our model does not account for these effects, and thus the validation of our model with IV measurements^{24,38} is not feasible. In addition, the IV response of the photoelectrode couples all physical processes with different time scales in a global photocurrent measurement. Thus, disentangling of the individual processes from the IV response is difficult, and it is usually achieved by spectroscopic methods⁴⁰ which probe response of the system to the spectrum of frequency perturbations.

We checked that the maximum photocurrent obtainable from the hematite electrode based purely on the number of absorbed photons is $qP = 12.5 \text{ mA/cm}^2$ for AM1.5G illumination, which is the theoretical maximum based on the bandgap of hematite under these illumination conditions. This value is also obtained for the Gärtner photocurrent eq 29 when the bracket term is close to one and also for the Reichmann photocurrent (that recovers the Gärtner photocurrent in the regime of large voltages). The plateau of the numerical photocurrent $j_{\text{h}}(0)$ cannot be computed here, because our model cannot be used to predict photocurrents at voltages higher than $V_{\text{r,RHE}} > V_{\text{r,RHE}}^{\text{inv}}$. At such voltages, an inversion layer is formed as described in the previous text and this would need degenerate statistics to be included in the model.

Cu_2O . We also applied our model to simulate charge transport in p-type semiconductors used as photocathodes. Appropriate changes in the equations were introduced, resulting from doping with acceptors rather than donors. Cuprous oxide (Cu_2O) is an abundant and promising material for the PEC photocathodes. The main issue with Cu_2O is its limited stability in water that is currently being addressed with the stabilizing overlayers.^{41–43} The downward band bending occurs when $V_{\text{r,RHE}}$ is more negative than $V_{\text{fb,RHE}}$. This leads to drift of electrons to the electrolyte, Figure 5. Upon illumination, the hole concentration is assumed to remain equal to the dark hole concentration. The electron concentration is calculated from the electron continuity equation. The electrons are accumulated near the SEI where they reduce water to H_2 with the rate constant k_{tre} .

In the case of p-type Cu_2O , the majority carriers are holes, and thus the counter electrode carries out the oxidation reaction (including the associated overpotential η). Although

the electron quasi-Fermi level E_{Fn} is negative with respect to E_{red} , making it suitable for hydrogen evolution, Figure 5, corrosion prevents hydrogen evolution in the experiment unless the Cu_2O is protected by overlayers.⁴¹ So far, our model does not consider corrosion; here we aimed at showing the general energetic configuration of the p-type PEC photoelectrode.

CONCLUSION

We presented a physical model for minority charge carrier transport in semiconductor PEC electrodes in contact with an electrolyte. The direct charge transfer to the electrolyte from valence or conduction band, band-to-band recombination, and Lambert–Beer optical generation were assumed. The numerical solution of the model equations allows us to calculate the minority carrier concentration and the quasi-Fermi level. Our resulting energy band diagram of the PEC cell accounts for the potential drop in the Helmholtz layer, and it is capable of modeling both band edge pinning and unpinning. The differences in the simulated and measured photocurrent are due to the nanostructure effects on the charge transport and light absorption, which are not included in our model. The numerical model was implemented in the interactive software tool that can be freely accessed online.²¹ All presented results of this work can be reproduced with this software, and we invite all members of the research community to use it while designing PEC cells. We are currently working on an extension of our model to a fully coupled drift-diffusion model with surface states. Such photoelectrode models need to accompany the experimental studies to suppress recombination losses (e.g., by the surface passivation) and enhance the charge transfer (e.g., by catalysis), the two major issues for efficient metal oxide photoelectrodes.⁴⁴

ASSOCIATED CONTENT

Supporting Information

Text detailing equations for Reichmann photocurrent and figures showing additional simulation results. This material is available free of charge via the Internet at <http://pubs.acs.org>.

AUTHOR INFORMATION

Corresponding Author

*E-mail: cend@zhaw.ch.

Notes

The authors declare no competing financial interest.

ACKNOWLEDGMENTS

We thank H. J. Lewerenz, G. Schlichthoerl, L. Bertoluzzi, F. T. Abdi, B. Klahr, and A. Rothschild for fruitful discussions. The financial support by the Swiss Federal Office of Energy (PECHouse2 project, Contract No. SI/500090-02) is gratefully acknowledged.

REFERENCES

- (1) Lewis, N. S.; Nocera, D. G. Powering the planet: Chemical challenges in solar energy utilization. *Proc. Natl. Acad. Sci. U. S. A.* **2006**, *103*, 15729–15735.
- (2) Schiermeier, Q. Renewable power: Germany's energy gamble. *Nature* **2013**, *496*, 156–158.
- (3) Khaselev, O.; Turner, J. A. A Monolithic Photovoltaic-Photoelectrochemical Device for Hydrogen Production via Water Splitting. *Science* **1998**, *280*, 425–427.
- (4) van de Krol, R.; Liang, Y. An n-Si/n- Fe_2O_3 Heterojunction Tandem Photoanode for Solar Water Splitting. *CHIMIA* **2013**, *67*, 168–171.
- (5) Sivula, K. Solar-to-Chemical Energy Conversion with Photoelectrochemical Tandem Cells. *CHIMIA* **2013**, *67*, 155–161.
- (6) Abdi, F. F.; Han, L.; Smets, A. H. M.; Zeman, M.; Dam, B.; van de Krol, R. Efficient solar water splitting by enhanced charge separation in a bismuth vanadate-silicon tandem photoelectrode. *Nat. Commun.* **2013**, *4*.
- (7) Krol, R. V. D.; Grätzel, M. *Photoelectrochemical Hydrogen Production*; Springer: Berlin, 2011.
- (8) Gärtner, W. W. Depletion-Layer Photoeffects in Semiconductors. *Phys. Rev.* **1959**, *116*, 84–87.
- (9) Wilson, R. H. A model for the current-voltage curve of photoexcited semiconductor electrodes. *J. Appl. Phys.* **1977**, *48*, 4292–4297.
- (10) Reichman, J. The current-voltage characteristics of semiconductor-electrolyte junction photovoltaic cells. *Appl. Phys. Lett.* **1980**, *36*, 574–577.
- (11) Andrade, L.; Lopes, T.; Ribeiro, H. A.; Mendes, A. Transient phenomenological modeling of photoelectrochemical cells for water splitting—Application to undoped hematite electrodes. *Int. J. Hydrogen Energy* **2011**, *36*, 175–188.
- (12) Foley, J. M.; Price, M. J.; Feldblyum, J. I.; Maldonado, S. Analysis of the operation of thin nanowire photoelectrodes for solar energy conversion. *Energy Environ. Sci.* **2012**, *5*, S203–S220.
- (13) Peter, L.; Li, J.; Peat, R. Surface recombination at semiconductor electrodes: Part I. Transient and steady-state photocurrents. *J. Electroanal. Chem. Interfacial Electrochem.* **1984**, *165*, 29–40.
- (14) Klahr, B.; Gimenez, S.; Fabregat-Santiago, F.; Hamann, T.; Bisquert, J. Water Oxidation at Hematite Photoelectrodes: The Role of Surface States. *J. Am. Chem. Soc.* **2012**, *134*, 4294–4302.
- (15) Bertoluzzi, L.; Bisquert, J. Equivalent Circuit of Electrons and Holes in Thin Semiconductor Films for Photoelectrochemical Water Splitting Applications. *J. Phys. Chem. Lett.* **2012**, 2517–2522.
- (16) Carver, C.; Ulissi, Z.; Ong, C.; Dennison, S.; Kelsall, G.; Hellgardt, K. Modelling and development of photoelectrochemical reactor for H_2 production. *Int. J. Hydrogen Energy* **2012**, *37*, 2911–2923.
- (17) Haussener, S.; Hu, S.; Xiang, C.; Weber, A. Z.; Lewis, N. Simulations of the irradiation and temperature dependence of the efficiency of tandem photoelectrochemical water-splitting systems. *Energy Environ. Sci.* **2013**, *6*, 3605–3618.
- (18) Salvador, P. Semiconductors' Photoelectrochemistry: A Kinetic and Thermodynamic Analysis in the Light of Equilibrium and Nonequilibrium Models. *J. Phys. Chem. B* **2001**, *105*, 6128–6141.
- (19) Memming, R. *Semiconductor Electrochemistry*; John Wiley & Sons: Hoboken, NJ, USA, 2008.
- (20) Peter, L. M. Energetics and kinetics of light-driven oxygen evolution at semiconductor electrodes: the example of hematite. *J. Solid State Electrochem.* **2013**, *17*, 315–326.
- (21) Cendula, P. The model is available freely on the internet (accessed Sep. 12, 2014). <http://icp.zhaw.ch/PEC>.
- (22) Swierk, J. R.; Mallouk, T. E. Design and development of photoanodes for water-splitting dye-sensitized photoelectrochemical cells. *Chem. Soc. Rev.* **2013**, *42*, 2357–2387.
- (23) Krol, R. v. d.; Liang, Y.; Schoonman, J. Solar hydrogen production with nanostructured metal oxides. *J. Mater. Chem.* **2008**, *18*, 2311–2320.
- (24) Dotan, H.; Sivula, K.; Grätzel, M.; Rothschild, A.; Warren, S. C. Probing the photoelectrochemical properties of hematite ($\alpha\text{-Fe}_2\text{O}_3$) electrodes using hydrogen peroxide as a hole scavenger. *Energy Environ. Sci.* **2011**, *4*, 958.
- (25) Klahr, B. M.; Hamann, T. W. Voltage dependent photocurrent of thin film hematite electrodes. *Appl. Phys. Lett.* **2011**, *99*, 063508-1–063508-3.
- (26) Bisquert, J.; Cendula, P.; Bertoluzzi, L.; Gimenez, S. Energy Diagram of Semiconductor/Electrolyte Junctions. *J. Phys. Chem. Lett.* **2014**, *5*, 205–207.

- (27) NREL. *Solar Spectral Irradiance: Air Mass 1.5* (accessed Mar. 17, 2012). <http://rredc.nrel.gov/solar/spectra/am1.5/>.
- (28) Tan, M. X.; Laibinis, P. E.; Nguyen, S. T.; Kesselman, J. M.; Stanton, C. E.; Lewis, N. S. In *Progress in Inorganic Chemistry*; Karlin, K. D., Ed.; John Wiley & Sons: New York, NY, USA, 1994; pp 21–144.
- (29) Markowich, P. A.; Ringhofer, C. A.; Schmeiser, C. *Semiconductor equations*; Springer-Verlag: New York, NY, USA, 1990.
- (30) Walter, M. G.; Warren, E. L.; McKone, J. R.; Boettcher, S. W.; Mi, Q.; Santori, E. A.; Lewis, N. S. Solar Water Splitting Cells. *Chem. Rev.* **2010**, *110*, 6446–6473.
- (31) Mills, T. J.; Lin, F.; Boettcher, S. W. Theory and Simulations of Electrocatalyst-Coated Semiconductor Electrodes for Solar Water Splitting. *Phys. Rev. Lett.* **2014**, *112*, No. 148304.
- (32) Kay, A.; Cesar, I.; Grätzel, M. New Benchmark for Water Photooxidation by Nanostructured Fe_2O_3 Films. *J. Am. Chem. Soc.* **2006**, *128*, 15714–15721.
- (33) Chen, Z.; Deutsch, T. G.; Dinh, H. N.; Domen, K.; Emery, K.; Forman, A. J.; Gaillard, N.; Garland, R.; Heske, C.; Jaramillo, T. F.; et al. *Photoelectrochemical Water Splitting*; Springer Briefs in Energy; Springer: New York, 2013; pp 7–16.
- (34) Nozik, A. J. Photoelectrochemistry: Applications to Solar Energy Conversion. *Annu. Rev. Phys. Chem.* **1978**, *29*, 189–222.
- (35) Grätzel, M. Photoelectrochemical cells. *Nature* **2001**, *414*, 338–344.
- (36) Hodes, G. Photoelectrochemical Cell Measurements: Getting the Basics Right. *J. Phys. Chem. Lett.* **2012**, *3*, 1208–1213.
- (37) Morrison, S. R. *Electrochemistry at semiconductor and oxidized metal electrodes*; Plenum Press: New York, NY, USA, 1980.
- (38) Tilley, S. D.; Cornuz, M.; Sivula, K.; Grätzel, M. Light-Induced Water Splitting with Hematite: Improved Nanostructure and Iridium Oxide Catalysis. *Angew. Chem.* **2010**, *122*, 6549–6552.
- (39) Upul Wijayantha, K.; Saremi-Yarahmadi, S.; Peter, L. M. Kinetics of oxygen evolution at $\alpha\text{-Fe}_2\text{O}_3$ photoanodes: A study by photoelectrochemical impedance spectroscopy. *Phys. Chem. Chem. Phys.* **2011**, *13*, 5264–5270.
- (40) Peter, L. *Photoelectrochemical Water Splitting: Materials, Processes and Architectures*; Royal Society of Chemistry: Cambridge, U.K., 2013.
- (41) Paracchino, A.; Laporte, V.; Sivula, K.; Grätzel, M.; Thimsen, E. Highly active oxide photocathode for photoelectrochemical water reduction. *Nat. Mater.* **2011**, *10*, 456–461.
- (42) Paracchino, A.; Mathews, N.; Hisatomi, T.; Stefiak, M.; Tilley, S. D.; Grätzel, M. Ultrathin films on copper(i) oxide water splitting photocathodes: a study on performance and stability. *Energy Environ. Sci.* **2012**, *5*, 8673.
- (43) Tilley, S. D.; Schreier, M.; Azevedo, J.; Stefiak, M.; Grätzel, M. Ruthenium Oxide Hydrogen Evolution Catalysis on Composite Cuprous Oxide Water-Splitting Photocathodes. *Adv. Funct. Mater.* **2014**, *24*, 303–311.
- (44) Sivula, K. Metal Oxide Photoelectrodes for Solar Fuel Production, Surface Traps, and Catalysis. *J. Phys. Chem. Lett.* **2013**, *4*, 1624–1633.
- (45) Paracchino, A.; Brauer, J. C.; Moser, J.-E.; Thimsen, E.; Grätzel, M. Synthesis and Characterization of High-Photoactivity Electrodeposited Cu_2O Solar Absorber by Photoelectrochemistry and Ultrafast Spectroscopy. *J. Phys. Chem. C* **2012**, *116*, 7341–7350.
- (46) Xu, Y.; Schoonen, M. A. A. The absolute energy positions of conduction and valence bands of selected semiconducting minerals. *Am. Mineral.* **2000**, *85*, 543–556.
- (47) Niu, M.; Huang, F.; Cui, L.; Huang, P.; Yu, Y.; Wang, Y. Hydrothermal Synthesis, Structural Characteristics, and Enhanced Photocatalysis of $\text{SnO}_2/\alpha\text{-Fe}_2\text{O}_3$ Semiconductor Nanoheterostructures. *ACS Nano* **2010**, *4*, 681–688.
- (48) Morin, F. J. Electrical Properties of $\alpha\text{-Fe}_2\text{O}_3$. *Phys. Rev.* **1954**, *93*, 1195–1199.
- (49) Cesar, I.; Sivula, K.; Kay, A.; Zboril, R.; Grätzel, M. Influence of Feature Size, Film Thickness, and Silicon Doping on the Performance of Nanostructured Hematite Photoanodes for Solar Water Splitting. *J. Phys. Chem. C* **2008**, *113*, 772–782.
- (50) Glasscock, J. A.; Barnes, P. R. F.; Plumb, I. C.; Bendavid, A.; Martin, P. J. Structural, optical and electrical properties of undoped polycrystalline hematite thin films produced using filtered arc deposition. *Thin Solid Films* **2008**, *516*, 1716–1724.
- (51) Bosman, A.; van Daal, H. Small-polaron versus band conduction in some transition-metal oxides. *Adv. Phys.* **1970**, *19*, 1–117.